Available online at www.sciencedirect.com

ScienceDirect

Procedia Structural Integrity 18 (2019) 330–346

Structural Integrity Procedia

www.elsevier.com/locate/procedia

25th International Conference on Fracture and Structural Integrity

# Investigation of the crack tip stress field in a stainless steel SENT specimen by means of Thermoelastic Stress Analysis

Giuseppe Pitarresi[a,*], Mauro Ricotta[b], Giovanni Meneghetti[b]

[a]*Università degli Studi di Palermo, Department of Engineering, Viale delle Scienze, 90128 Palermo – Italy*
[b]*University of Padova, Department of Industrial Engineering, Via Venezia, 1, 35131 Padova – Italy*

**Abstract**

In this work a *Thermoelastic Stress Analysis* (TSA) setup is implemented to investigates the *Thermoelastic* and *Second Harmonic* signals on a fatigue loaded *Single Edge Notched Tension* (SENT) specimen made of stainless steel AISI 304L. Three load ratios are in particular applied, $R$=-1, 0, 0.1. The thermoelastic signal is used to evaluate the Stress Intensity Factor via two approaches, the Stanley-Chan linear interpolation method and the over-deterministic least-square fitting (LSF) method using the Williams' series expansion. Regarding least-square fitting, an iterative procedure is proposed to identify the optimal crack tip position in the thermoelastic maps. The SIF and T-Stress are then evaluated considering the influence of the number of terms (up to 20) in the Williams' series function, and the extent and position of the area used for data input. The study also investigates the *Second Harmonic* signal observed on the wake of the crack with varying load ratio $R$. An interpretation is proposed that considers the rise of the Second Harmonic as the result of the modulation of the compression loads between the crack flanks, rather than dissipation phenomena. This interpretation enables the possibility to use this parameter to reveal the presence and extent of crack-closure.


Peer-review under responsibility of the Gruppo Italiano Frattura (IGF) ExCo.

*Keywords,* Thermoelastic Stress Analysis, Least Square Fitting, Stress Intensity Factor, Crack Closure, T-Stress

* Corresponding author. Tel.: +39 091 23897281.
*E-mail address:* giuseppe.pitarresi@unipa.it

2452-3216 
Peer-review under responsibility of the Gruppo Italiano Frattura (IGF) ExCo.
10.1016/j.prostr.2019.08.173

## 1. Introduction

Thermoelastic Stress Analysis (TSA) is a full-field non-contact technique by means of which the in-plane stress field is correlated to temperature changes. These are measured on the surface of the body while this is subject to dynamic loading. The technique relies on the linear formulation of the Thermoelastic Effect,

$$\Delta T = -T_o \kappa \Delta \left( \sigma_{xx} + \sigma_{yy} \right) = A \Delta I \tag{1}$$

where $\Delta T$ is the temperature change induced by the Thermoelastic Effect under adiabatic conditions and linear elastic material behavior. In Eq. (1) $T_o$ is the initial body temperature, $\kappa$ a material specific thermoelastic constant and the stress term is the range of variation of the first stress invariant $\Delta I$ (see Pitarresi and Patterson (2003)) for a more in-depth review of the analytical derivation of Eq. (1)). If loading is modulated at a single frequency (cyclic sinusoidal loading), then $\Delta T$ can be measured as the amplitude of the harmonic at the load frequency (or *first harmonic*). Therefore, the thermoelastic signal can be obtained from harmonic content filtering of the sampled temperature *vs* time. This is usually performed with lock-in digital cross-correlation, but alternative approaches are also Least Square Fitting and Discrete Fourier Transform (Pitarresi (2015)).

TSA then provides a full field map of the sum of normal in-plane stresses (i.e. the first stress invariant). In presence of a crack, this information can be used to evaluate fracture mechanics parameters. In particular, several works have focused on the evaluation of the Stress Intensity Factor (SIF or $K$), proposing a number of approaches which have been mostly reviewed in Tomlinson and Olden (1999). An essential overview of the proposed methodologies identifies three general approaches,

- Direct interpolation methods;
- Methods based on the geometrical features of the cardioid isopachic contour;
- Over-Deterministic Methods based on Least Square Fitting (LSF) of analytical stress functions providing the elastic stress field at a crack.

Direct interpolation or extrapolation approaches are generally based on the Westergaard's equations arrested to the singular stress term. They are then restricted to operate in the nearest vicinity of the crack tip, and have the advantage to extrapolate the SIF by simple linear regressions of the thermoelastic signal versus geometrical variables (Pukas (1987)). The Stanley-Chan approach, first proposed in Stanley and Chan (1986), is perhaps the most popular, for its straightforward implementation. It presents the significant advantage of not requiring the identification of the crack tip location. On the other end, the influence of the constant T-Stress term has to be neglected, see e.g. Stanley and Dulieu-Smith (1996).

Methods based on the cardioid reconstruction have considered the T-Stress, but this has to be evaluated with specific data reduction procedures (Stanley and Dulieu-Smith (1996); Dulieu-Barton et al. (2000)).

Over-Deterministic Methods (ODM) use series expansion formulations of the Airy stress function evaluating the crack tip stress field. The most popular series stress functions that have been employed are those ascribed to, Williams (Lesniak and Boyce (1995); Ju et al. (1997); Zanganeh et al. (2008); Vieira et al. (2018)), Mushkelishvili (Tomlinson et al. (1997a); Díaz et al. (2004a); Diaz et al. (2004b)), Lekhnitskii (Lin et al. (1997); He and Rowlands (2004); Haj-Ali et al. (2008); Ju et al. (2010)). The Lekhnitskii's solution extends the application to media with orthotropic behavior.

Such formulations, all based on LSF, allow considering the influence of higher order coefficients, and then extend the zone ahead of the crack tip that can be effectively included for the least square fitting of experimental data. Once the stress function terms are obtained, another outcome of the analysis is the determination of single stress components (i.e. stress separation), which can be used for further analyses such as the evaluation of the J-Integral (Lin et al. (2015)). A common drawback of over-deterministic least-square fitting methods is the need to identify the crack tip location with good accuracy. One way to obtain a good estimation of the crack-tip is by picking the point that provides the minimal error or the best fit. This can be done by evaluating statistically based fitness parameters, or by including the crack tip position as a further unknown term to be determined with LSF (Diaz et al. (2004a); Vieira et al. (2018)).

Some authors have also proposed a direct crack tip identification from the phase map of the thermoelastic signal, exploiting some peculiar thermoelastic features characterising the fracture process zone. Generally, this provides a coarse localisation, that can be used as a seed point to more accurate recursive LSF algorithms (Diaz et al. (2004a); Díaz et al. (2004b)).

Some more recent works have explored the use of the experimental SIF and crack tip localisation from TSA to characterise the full Paris' law of the material, by a purely elastic approach (Jones et al. (2010); Bar and Seifert (2014); Ancona et al. (2016)), or a combined elastic-plastic analysis (Meneghetti et al. (2019)). The Thermoelastic phase and the Second Harmonic signal have been also investigated as potential indicators of damage onset and energy dissipation due to plastic work (Palumbo et al. (2017); Urbanek and Bär (2017)).

The present work investigates the crack-tip stress field of a Single Edge Notched Tension (SENT) sample made of a stainless steel AISI 304L. Three different load ratios $R$=-1, 0, 0.1 have been applied to investigate the influence of crack-closure and crack compression on the thermoelastic maps. The SIF and the T-stress have been derived with the direct interpolation method of Stanley-Chan (Stanley and Chan (1986)) and with an over-deterministic LSF of the Williams' series stress solution. Some noteworthy outputs of the performed investigation include,

- The evaluation of an iterative procedure to localize the crack tip position from TSA maps, based on optimizing a coefficient of determination $R^2$ of the LSF;
- The analysis of the influence of the number of terms retained in the William's solution (up to 20), and of the extent of the data input area, in the least-square fitting results of SIF and T-stress;
- The evaluation of the influence of a negative R-ratio and crack-closure on the evaluation of the experimental SIF;
- The analysis of the *second harmonic* signal as a parameter sensitive to crack-closure. An explanation is in particular proposed regarding the interpretation of the features of the *second harmonic* signal observed on the wake of the crack.

## 2. Experimental set-up

### *2.1. Sample preparation and plan of experiments*

The sample tested in this work is a Single Edge Notched Tension coupon with a machined 90° V-notch, made of stainless steel AISI 304L (dimensions are reported in Fig. 1). A natural crack starting from the V-notch was grown under fatigue loading, applying a sinusoidal cyclic load between 1 and 10 kN at 20 Hz. Fatigue propagation was allowed up to a crack length of about a/W=0.5 before stating the acquisition of temperature for TSA. The sample face exposed to the IR camera was painted with a matt black paint to enhance and uniform infrared emissivity. Each TSA acquisition had a duration of 30 sec, within which the sampled temperature was stored for the successive off-line processing.

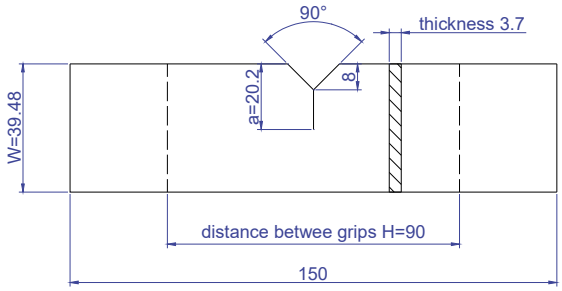


Fig. 1. Sketch of the tested SENT sample (dimensions in [mm]).

Tests were performed on a servo-hydraulic MTS 810 testing machine, under load control. Sinusoidal cyclic loading was applied with three different load-ratios $R$, -1 (-4.5 to 4.5 kN); $R$=0 (0 to 9 KN); $R$=0.1 (1 to 10 kN). Each load ratio was applied in seven successive acquisitions, differing only for the loading frequency that was sequentially set

at 1,2,3,5,10,15,20 Hz, for a total number of 3×7=21 acquisitions. In order to control that no significant crack growth occurred during the 30 sec acquisitions, a reflex digital camera with a macro lens was used to measure the crack length from the sample face opposite to that stared by the IR camera. The photos of the optical camera, taken for each TSA acquisition, have a spatial resolution of 10 μm/pixel, and were used to obtain a reference the crack-tip position. During the time occurred to acquire the 21 TSA sequences the cyclic loading was not stopped, in order to preserve the most self-similar conditions. This produced a slight growth of the crack, accumulated during this time. The $a/W$ ratio measured in each of the three sets of acquisition was, 0.51 for R=-1, 0.52 for R=0 and 0.53 for R=0.1, with a total crack growth of about 0.5 mm. The maximum crack growth during a 30 sec acquisition was 0.11 mm (measured with R=0.1 and load frequency of 20 Hz).

### *2.2. Thermographic setup and implementation of TSA*

The IR camera employed is a cooled sensor FLIR X6540sc. The model used in this work mounted a 50 mm focus f# 2.0 lens (allowing for a field-of-view of 10.97°×8.78°), positioned at a distance resulting in a geometric resolution (size of one pixel on the specimen or *ifov*) of 0.15 mm/px. In all the TSA acquisitions, the sampling frequency was set at 200 Hz and the integration time at 659 μsec.

During the registration of thermograms a reference sinusoidal signal, derived from the load signal generator of the testing machine digital controller, was fed into the lock-in input ingress of the IR camera. This allowed the *.ptw* files to be post-processed into FLIR THESA, evaluating the thermoelastic first and second harmonic maps.

The same maps have been obtained by employing an in-house developed Matlab script which applies the Discrete Fourier Transform to the sampled frames (Pitarresi 2015). This allowed to evaluate the whole frequency content of the temperature signal at each point, and extract a self-reference signal for digital cross-correlation. Both the in-house DFT filtering and the THESA cross-correlation yielded the same quantitative results.

The material thermoelastic constant $\kappa$ had been evaluated experimentally in a previous work (Meneghetti, Ricotta, and Atzori 2016), and results in $\kappa$=3.75·10$^{-6}$ MPa$^{-1}$. This was used here to rescale the measured temperature, which was available from the internal IR camera calibration, into stresses, according to Eq (1).

## 3. Stress Intensity Factor calculation

### *3.1. Stanley-Chan extrapolation procedure*

Stanley and Chan used the Westergaard's solutions to derive an analytical expression correlating the maximum value of $\Delta I = A\Delta T$ along a scanline parallel to the crack line, and $y$, i.e. the distance of the scanline from the crack-line. The final relationship can be written as,

$$y = \frac{3\sqrt{3}\Delta K_I^2}{4A^2\pi}\left[\Delta T_{max} + \frac{\Delta\sigma_{xo}}{A}\right]^{-2} \tag{2}$$

where $A=(T_o\kappa)^{-1}$ is the stress calibration thermoelastic constant. After neglecting the T-stress $\sigma_{xo}$ in Eq. (2), it is seen that $K_I$ can be derived from the slope of a linear regression between values of $y$ versus $(1/\Delta T_{max})^2$. $\Delta T_{max}$ is the maximum thermoelastic signal along a scanline $y=cost.$, and is easily retrieved from the thermoelastic map. Moreover, only relative values of $\Delta y$ matter in the calculation of the slope, so that the identification of the crack tip location is not needed. Therefore, the implementation of the Stanley-Chan procedure is rather straightforward, requiring only an estimation of the SIF dominated region of linear behavior, which is usually manually performed after looking at data plots such as the one in fig. 2a.

### *3.2. Williams series stress function and least square fitting*

The Williams' series expansion of stress components used for the least square fitting of experimental data has been implemented in several works and with different techniques, comprising also Photoelasticity or Digital Image

Correlation (Ramesh et al. (2002)). The adaptation to the first stress invariant in TSA is straightforward, yielding the following expression for Mode I only,

$$\Delta T = \frac{1}{A}\cdot\left(\sigma_{xx}+\sigma_{yy}\right) = \frac{1}{A}\cdot\sum_{n=1}^{\infty} A_{In}\left[2nr^{\frac{n}{2}-1}\cos\left(\frac{n}{2}-1\right)\vartheta\right] \tag{3}$$

where $A_{In}$ indicates the unknown terms of the series. Arranging Eq. (3) as a matrix expression yields,

$$\frac{1}{A}\cdot\begin{bmatrix}\cdots\\ \left(\Delta T\right)_i\\ \cdots\end{bmatrix}_{i\times 1} = \begin{bmatrix}\cdots & \cdots & \cdots & \cdots & \cdots\\ \frac{2}{\sqrt{r_i}}\cos\left(\frac{\vartheta_i}{2}\right) & 4 & 6\sqrt{r_i}\cos\left(\frac{\vartheta_i}{2}\right) & 8r_i & \cdots\\ \cdots & \cdots & \cdots & \cdots & \cdots\end{bmatrix}_{i\times n} \times \begin{bmatrix}\Delta A_{I1}\\ \Delta A_{I2}\\ \Delta A_{I3}\\ \Delta A_{I4}\\ \cdots\end{bmatrix}_{n\times i} \tag{4}$$

where $i$ is the number of input data points, and the $i\times n$ matrix shows only the first four terms of Williams' series, for clarity of representation. In this work, the linear matrix Eq. (4) is solved in Matlab by using the backslash '\' operator (Alshaya and Rowlands (2017)). Arresting the Williams' solution to the first two terms yields an expression that is formally similar to that of Westergaard,

$$\Delta\left(\sigma_{xx}+\sigma_{yy}\right) = A\Delta T = \frac{2\Delta K}{\sqrt{2\pi r}}\cos\left(\vartheta/2\right) - \Delta\sigma_{xo} \tag{5}$$

Therefore, the SIF and T-stress are readily derived from the first two terms $\Delta A_{I1}$ and $\Delta A_{I2}$, as follows,

$$\Delta K = \Delta A_{I1}\sqrt{2\pi};\ \Delta\sigma_{xo} = -4\Delta A_{I2} \tag{6}$$

In this work, the input data considered in the least square fitting belong to an annulus sector area (or data input area) as shown in Fig. 2b. This is centered on the crack tip, has inner radius $r_{min}$ and outer radius $r_{max}$, and an angular stretch from 22.5° to 157.5° (counterclockwise from the crack line). The influence of the data points on the SIF and T-stress is investigated by modifying the values of $r_{min}$ and $r_{max}$, while the stretching angle is kept constant.

In order to evaluate the effectiveness of fitting after changing the values of $r_{min}$ and $r_{max}$ and/or the number of terms in the Williams' model, a fitness parameter is proposed that is the coefficient of determination, or R-squared, $R^2$, as defined in linear regression fitting. This is computed by the following expression,

$$R^2 = 1 - \frac{RSS}{TSS} = 1 - \frac{\sum_i\left(\Delta T_i - \Delta T_{Wi}\right)^2}{\sum_i\left(\Delta T_i - mean\left(\Delta T_i\right)\right)^2} \tag{7}$$

where $RSS$ is the residual sum of squares, $TSS$ the total sum of squares, $\Delta T_i$ the measured value at point $i$, $\Delta T_{Wi}$ the predicted value from Williams' model and the $mean(\Delta T_i)$ the overall mean of measurements.

### *3.3. FEM evaluation*

In order to have a reference value for the Mode I Stress Intensity Factor (SIF) ranges, $\Delta K = K_{max} - K_{min}$, a finite element analysis was performed for the different crack lengths, taking advantage of the Peak Stress Method (Meneghetti and Lazzarin (2007)). In particular, linear elastic, two-dimensional, plane stress finite element analyses were performed by using the 4-node PLANE 182 element of ANSYS® commercial software and the "simple enhanced strain" element

formulation. To account for the machine grip effect in the numerical model, displacements were applied on the grip section (dotted lines in Figure 1).

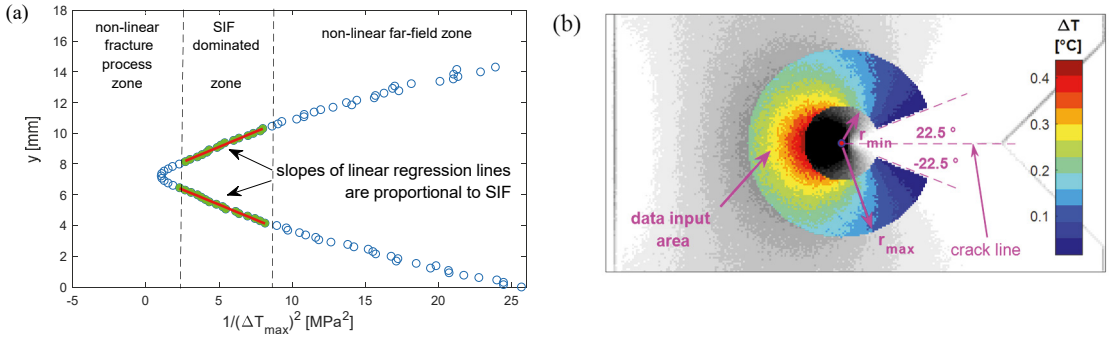


Fig. 2. (a) Experimental Stanley-Chan linear regression data plot (example taken from the SENT sample tested at $R$=0.1 and load frequency of 15 Hz); (b) definition of the *data input area* used in the LSF.

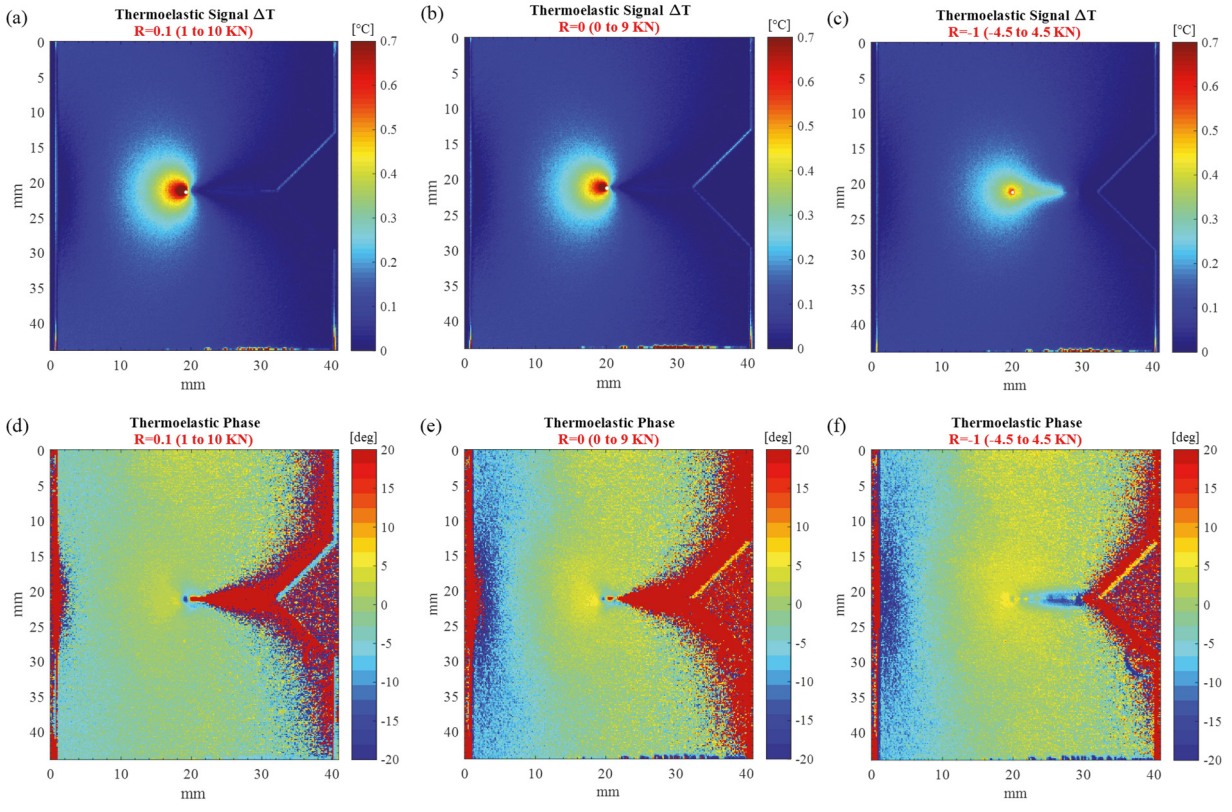


Fig. 3. Thermoelastic signal (a,b,c) and thermoelastic phase (d,e,f) maps acquired with load ratios R of 0.1 (a,d), 0 (b,e) and -1 (c,f). The white dot in (a,b,c) indicates the crack-tip location as measured by the optical camera. The data shown come from tests at load frequency of 15 Hz.

## 4. Results and discussion

### *4.1. Thermoelastic first-harmonic signals*

The thermoelastic signal is obtained from the temperature harmonic component at the loading frequency, here also referred to as *first-harmonic*. Such signal is characterized by a ΔT range (i.e. twice the amplitude of the harmonic) and a phase. Figure 3 shows the thermoelastic signal maps obtained for the three load ratio cases of R=0.1, 0, -1.

The maps in Fig. 3 indicate a significant difference between isopachic with R=-1 and isopachics with either R=0.1 or 0, with only R≥0 giving rise to the typical cardioid shape. In the case of R=-1 a significant thermoelastic signal is developed on the wake of the crack, which vanishes progressively moving from the crack tip towards the notch tip. It is interesting how such compression progressively vanishes before reaching the notch tip. This could be due to plasticity induced crack-closure, hampering the crack flanks to press uniformly, and to close the crack completely.

The phase maps also shows some different features along the crack flanks and ahead of the crack tip. It is finally noticed that in the case of R=0, in the zone immediately behind the crack tip, the phase signal shows some similarities to the case of R=-1, which might arise from an incipient crack closure.

### *4.2. Evaluation of SIF by the Stanley-Chan linear regression*

The procedure outlined in Section 2.2, and graphically exemplified in Fig. 2a, was applied to evaluate Δ*K* for each load ratio and each applied loading frequency. Results are collected in Table 1 and Figure 4. Furthermore, Figure 5 reports a close-up image of the phase map at the crack tip, for the case R=0.1, and varying load frequency. In general, it is observed that load frequencies above 5 Hz yield a quasi-constant value of Δ*K*, which can be taken as a proof of the onset of adiabaticity in each test. The relatively low threshold frequency is believed to be the effect of a relatively small heat diffusion constant for the tested steel. As the load frequency decreases, Fig. 5 shows that the zone with a significant phase shift at the crack tip increases. This confirms that such phase shifting is related to non-adiabatic phenomena, even if localized plasticity can also contribute. Since the load range is not varying, the plastic zone is expected to be self-similar in all tests of Fig. 5, therefore the significant increase of the phase-shifted zone is to be mainly ascribed to the progressively more difficult onset of adiabatic behavior with decreasing load frequency.

Table 1.Values of Δ*K* in [MPa×m$^{0.5}$] from the Stanley-Chan procedure.

| load frequency | 1 Hz | 2 Hz | 3 Hz | 5 Hz | 10 Hz | 15 Hz | 20 Hz | mean±st.dev (5,10,15,20 Hz) | FEM |
|---|---|---|---|---|---|---|---|---|---|
| *R*=0.1 | *23.34* | *25.17* | *26.9* | *26.56* | *27.78* | *26.96* | *27* | *27.08±0.5* | *22.64* |
| *R*=0 | *22.79* | *24.56* | *26.2* | *26.8* | *26.66* | *26.83* | *26.49* | *26.7±0.1* | *22.22* |
| *R*=-1 | *19.76* | *19.58* | *21.34* | *21.4* | *21.61* | *21.29* | *21.22* | *21.38±0.2* | *21.78* |

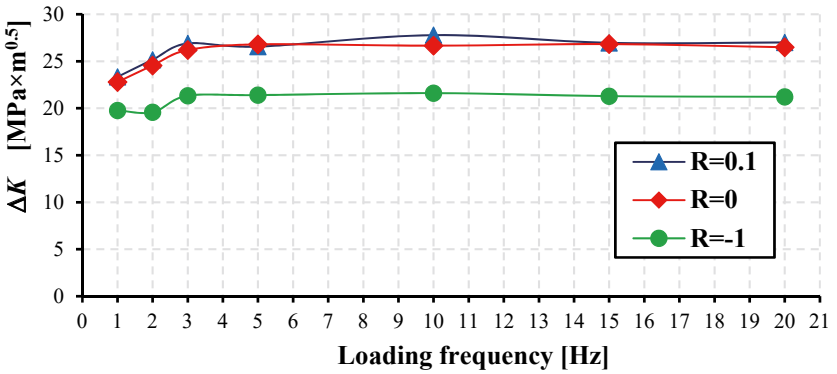


Fig. 4. Plot of Δ*K* with varying load frequency, from the Stanley-Chan procedure.

Results show also that there seem to be not a significant difference in $\Delta K$ between R=0.1 and R=0. This is somewhat in contrast with the earlier postulated presence of some crack-closure at R=0. In fact, crack-closure should reduce the value of the effective $\Delta K$. The value of $\Delta K$ at R=-1 is instead lower than that at R=0.1 of about 21 %. In this case, there is a significant effect of crack-closure induced by the half cycle compression load.

From Table 1 it is also seen that the values of $\Delta K$ obtained from the Stanley-Chan procedure in the case of R=0.1 and 0 are about 23% higher than the FEM estimations. It is recalled here that the potential influence of the T-Stress is not taken into account in the Stanley-Chan linear fitting. To the authors' knowledge, there is no work in the literature that has tried to quantify the impact of such omission. The plot of data in Fig. 2a evidences the presence of a mid-zone with a linear trend. Such a zone was clearly identified in all tests, and is apparently not eliminated by the presence of crack-closure and the application of negative load ratios. Also the omission of the T-Stress does not influence the linear trend of Eq. (2), since $\Delta\sigma_o$ is constant. It is observed here that the introduction of a negative T-Stress would have the effect of reducing the measured values of $\Delta K$. In particular, a value of $\Delta\sigma_o$ can be introduced in Eq. (2) that brings the experimental $\Delta K$ to coincide with the FEM prediction. In the cases or R=0.1 and 0, such value of $\Delta\sigma_o$ is about -60 MPa. A numerical T-Stress solution for an edge cracked rectangular plate subject to tension is provided by Fett (1998). By considering the case of a long plate ($H/W$>1.5), the estimation of $\Delta\sigma_o$ provided by Fett for the present $a/W$ values is about -22 MPa. Even if this value is about one third then the one estimated earlier, it is interesting to notice that the two estimations have both negative sign.

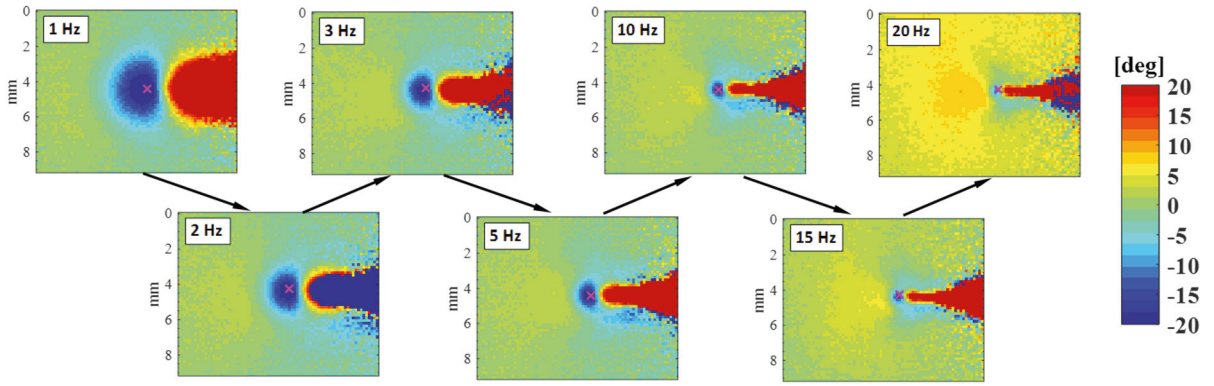


Fig. 5. Close-ups of phase map with varying load frequency from the test at R=0.1.

### *4.3. Evaluation of SIF by multipoint over-deterministic Least Square Fitting*

#### *4.3.1. Identification of the crack tip location*

The LSF procedure is renowned to require an accurate estimation of the crack tip location, to compute reliable values of $r$ and $\vartheta$. In this work, an initial iterative procedure is performed to identify the crack tip. A coarse estimation is initially made by identifying the crack tip position from the thermoelastic phase, as proposed by (Díaz et al. 2004). This location is used as a seed point for the iterative procedure. A square subset of $n\times n$ points, centered on the seed point, is considered. Least-square is then performed iteratively, each time considering a pixel of the subset as the provisional crack tip. The definitive crack tip position is taken as the one yielding the higher value of $R^2$, as defined by Eq. (7). From the above, it is then obvious that the proposed procedure cannot achieve a better accuracy than one pixel size.

In the present work the subset side chosen is $n$=11 pixels. The data input area has a fixed value of $r_{max}$=25 px, which is the typical further $y$-distance from the crack chosen in the Stanley-Chan regressions of Section 2. The $n\times n$ iteration is repeated with values of $r_{min}$ ranging between 1 px and 10 px, and for a number of Williams' terms ranging between 1 and 10, for a total number of least square evaluations of 11×11×10×10=12100, which are performed in Matlab in few seconds. The crack tips thus identified have been compared with the crack tip location measured by the optical camera, whose higher resolution provides a reliable reference. Some results are reported in Table 1. It is found that

the higher error is usually occurring along the $x$ coordinate, i.e. the vertical distance $\Delta y$ between the optical and the calculated crack tips is generally zero. Regarding the cases of R=0 and R=0.1, it is seen that the maximum error is $\Delta x$=5 px, and it generally occurs for low values of $r_{min}$, probably due to the blunting effect of plasticization. The error increases also with a number of Williams' terms above 6, probably due to the better ability of the model to adapt the plastic zone. Generally, though, when $r_{min}$ becomes higher than 5 px the error is almost always null, or limited to one pixel, indicating that the proposed iterative crack-tip search is effective.

Figure 6 shows close-ups of the crack-tip zone, with the position of the crack tip obtained from the iterative LSF algorithm, on both the $\Delta T$ and phase maps, and for the three load ratios. With regards to the phase maps (Fig. 6d,e,f, it is generally found that the predicted crack tip falls within the zone of local negative phase, although its exact position does not coincide necessarily with the beginning of such zone, as often pointed out in the literature.

Table 2. Maximum error in pixels between the crack-tip predicted by the iterative LSF and that measured by the optical camera ($r_{max}$=25 px).

| Number of Williams' terms | 1 | | | 2 | | | 3 | | | 4 | | | 5 | | | 6 | | | 8 | | | 10 | | |
|---|---|---|---|---|---|---|---|---|---|---|---|---|---|---|---|---|---|---|---|---|---|---|---|---|
| $r_{min}$ [px] | 1 | 5 | 10 | 1 | 5 | 10 | 1 | 5 | 10 | 1 | 5 | 10 | 1 | 5 | 10 | 1 | 5 | 10 | 1 | 5 | 10 | 1 | 5 | 10 |
| $R$=0.1 | *0* | *0* | *-1* | *0* | *0* | *0* | *0* | *0* | *0* | *0* | *0* | *0* | *0* | *0* | *0* | *-1* | *0* | *-1* | *-3* | *0* | *-1* | *-2* | *0* | *-1* |
| $R$=0 | *0* | *0* | *0* | *0* | *1* | *0* | *0* | *1* | *0* | *0* | *0* | *0* | *-1* | *0* | *0* | *-5* | *0* | *0* | *-3* | *0* | *0* | *-3* | *-1* | *-1* |
| $R$=-1 | *5* | *5* | *5* | *5* | *5* | *5* | *2* | *5* | *5* | *1* | *2* | *5* | *1* | *1* | *5* | *0* | *1* | *5* | *-1* | *2* | *5* | *0* | *3* | *5* |

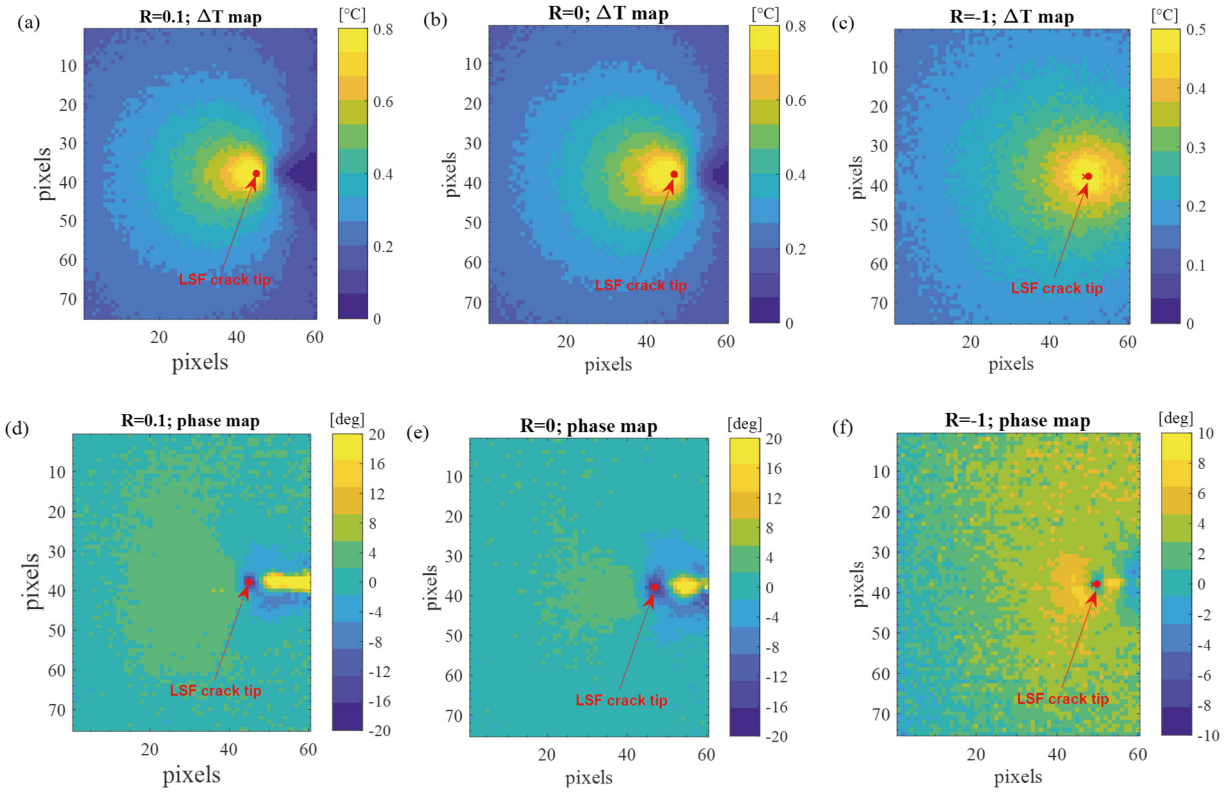


Fig. 6. Close-up images of the crack-tip zone with indication of the crack tip position obtained with the iterative LSF procedure.

*4.3.2. Evaluation of the SIF and T-Stress*

The investigation on the SIF and T-Stress is carried out by fixing the inner radius of the data input area to, $r_{min}$=5 px and evaluating four values of $r_{max}$=18, 24, 43, 116 px, which correspond to dimensionless values of 0.15, 0.20, 0.35, 0.95 if normalized by the ligament (distance between the crack tip and the straight edge, *W-a*). It is observed that the value of $r_{min}$=5 px follows from the previous analysis on the crack tip location, where such value of $r_{min}$ handed out a good match between predicted and measured crack tip positions. Such value of $r_{min}$ is also in good accordance with the value of $\Delta y$, around the crack tip, exhibiting non-linear behavior in the Stanley-Chan plot (e.g. see Fig. 2a). Moreover, the present evaluation is carried out on thermoelastic maps acquired with load frequencies above 10 Hz. From Section 4.2 and Fig. 5 it is seen that a radius of 5 px is already sufficient to avoid the near crack tip zone affected by a significant phase shift.

The values of $\Delta K$ and T-Stress variation $\Delta\sigma_o$ are reported in Tables 3,4,5 for R=0.1, 0, -1, respectively. Results are reported up to a number of Williams' terms, $N_W$, of 10. Higher values of $N_w$ did not produce meaningful differences and $N_w$=10 can then be considered as a convergence value for the present application. The value of $R^2$ from Eq. (7) is also reported for each evaluation. In general, the value of $R^2$ is always higher than 0.95 with $N_W$ above 3 (see also Fig. 7a). The value of $R^2$ is computed considering only the *data input area* (see fig. 2b). Therefore, high values of $R^2$ indicate only a good fitness of the model to the experimental data limited to such confined area.

Regarding the values of $\Delta K$, it is observed that they are significantly affected by both the number of Williams' terms $N_w$ used in the fitting and the outer extension of the data input area. In particular there is a constant increase of $\Delta K$ with $r_{max}$ for values of $N_w$ higher than 3 (see Fig. 7b). It is useful to make a visual comparison of the contour plots of experimental and least-square fit isopachics as proposed in Fig. 8. A small $r_{max}$ determines a rather bad matching of isopachics lower than $I$=350 MPa, as shown in Fig. 8a. As $r_{max}$ increases, the matching gradually improves far from the crack tip (Fig. 8b,c) but worsens near the crack tip (Fig. d). The matching observed in Fig. 8c, relative to a wide data input area and high $N_w$, shows that the Williams' model is able to reproduce fairly well the stress field far from the crack tip.

Table 3. Values of SIF and T-Stress for R=0.1 from the LSF method ($r_{min}$=5 px; $r_{max}$=18, 24, 43, 116 px).

| Number of Williams' terms | 1 | 2 | 3 | 4 | 5 | 6 | 8 | 10 | 12 | FEM |
|---|---|---|---|---|---|---|---|---|---|---|
| $r_{max/(W-a)}$=0.15; number of input data points=804 | | | | | | | | | | |
| $R^2$ | *0.9811* | *0.9819* | *0.9835* | *0.9911* | *0.9911* | *0.9928* | *0.9928* | *0.9928* | *0.9928* | |
| $\Delta K$ [MPa×m$^{0.5}$] | *25.13* | *24.49* | *23.75* | *21.13* | *21.16* | *19.88* | *20.26* | *20.73* | *20.73* | *22.64* |
| $\Delta\sigma_0$ [MPa] | *0.00* | *-9.91* | *-2.68* | *-107.06* | *-105.73* | *-190.92* | *-162.99* | *-115.47* | *-115.47* | |
| $r_{max/(W-a)}$=0.20; number of input data points=1508 | | | | | | | | | | |
| $R^2$ | *0.982* | *0.9826* | *0.9836* | *0.9907* | *0.9908* | *0.9914* | *0.9914* | *0.9914* | *0.9914* | |
| $\Delta K$ [MPa×m$^{0.5}$] | *25.10* | *25.70* | *25.20* | *22.69* | *22.51* | *21.80* | *21.56* | *22.52* | *22.52* | *22.64* |
| $\Delta\sigma_0$ [MPa] | *0.00* | *8.28* | *14.69* | *-75.32* | *-83.41* | *-126.36* | *-144.09* | *-59.49* | *-59.49* | |
| $r_{max/(W-a)}$=0.35; number of input data points=5005 | | | | | | | | | | |
| $R^2$ | *0.971* | *0.9853* | *0.9863* | *0.9878* | *0.9881* | *0.9884* | *0.9887* | *0.9887* | *0.9887* | |
| $\Delta K$ [MPa×m$^{0.5}$] | *24.11* | *27.10* | *27.45* | *26.28* | *25.90* | *25.47* | *24.49* | *24.80* | *25.36* | *22.64* |
| $\Delta\sigma_0$ [MPa] | *0.00* | *32.69* | *26.55* | *-6.96* | *-20.73* | *-41.35* | *-96.06* | *-73.24* | *-27.71* | |
| $r_{max/(W-a)}$=0.95; number of input data points=35093 | | | | | | | | | | |
| $R^2$ | *0.8083* | *0.8655* | *0.9424* | *0.9549* | *0.9744* | *0.9826* | *0.9878* | *0.9887* | *0.9888* | |
| $\Delta K$ [MPa×m$^{0.5}$] | *19.38* | *25.24* | *27.57* | *30.72* | *27.90* | *30.18* | *28.70* | *27.58* | *27.05* | *22.64* |
| $\Delta\sigma_0$ [MPa] | *0.00* | *41.40* | *2.75* | *64.89* | *0.61* | *72.85* | *26.53* | *-25.68* | *-55.44* | |

Regarding the values of $\Delta K$, it is observed that they are significantly affected by both the number of Williams' terms $N_w$ used in the fitting and the outer extension of the data input area. In particular there is a constant increase of $\Delta K$ with $r_{max}$ for values of $N_w$ higher than 3 (see Fig. 7b). It is useful to make a visual comparison of the contour plots of experimental and least-square fit isopachics as proposed in Fig. 8. A small $r_{max}$ determines a rather bad matching of isopachics lower than $I$=350 MPa, as shown in Fig. 8a. As $r_{max}$ increases, the matching gradually improves far from the crack tip (Fig. 8b,c) but worsens near the crack tip (Fig. d). The matching observed in Fig. 8c, relative to a wide data input area and high $N_w$, shows that the Williams' model is able to reproduce fairly well the stress field far from the crack tip.

Table 4. Values of SIF and T-Stress for R=0 from the LSF method ($r_{min}$=5 px; $r_{max}$=18, 24, 43, 116 px).

| Number of Williams' terms | 1 | 2 | 3 | 4 | 5 | 6 | 8 | 10 | 12 | FEM |
|---|---|---|---|---|---|---|---|---|---|---|
| $r_{max/(W-a)}$=0.15; number of input data points=804 | | | | | | | | | | |
| $R^2$ | *0.9769* | *0.9813* | *0.9814* | *0.9902* | *0.9906* | *0.9927* | *0.9927* | *0.9928* | *0.9928* | |
| $\Delta K$ [MPa×m$^{0.5}$] | *26.28* | *24.72* | *24.78* | *21.92* | *21.44* | *19.99* | *19.28* | *20.20* | *20.20* | *22.22* |
| $\Delta\sigma_0$ [MPa] | *0.00* | *-24.26* | *-24.83* | *-138.56* | *-162.82* | *-258.67* | *-313.88* | *-220.57* | *-220.57* | |
| $r_{max/(W-a)}$=0.20; number of input data points=1508 | | | | | | | | | | |
| $R^2$ | *0.9819* | *0.9819* | *0.982* | *0.9906* | *0.9912* | *0.9922* | *0.9924* | *0.9924* | *0.9924* | |
| $\Delta K$ [MPa×m$^{0.5}$] | *26.17* | *26.05* | *26.16* | *23.35* | *22.80* | *21.82* | *20.90* | *21.01* | *21.01* | *22.22* |
| $\Delta\sigma_0$ [MPa] | *0.00* | *-1.61* | *-3.01* | *-103.83* | *-128.90* | *-187.81* | *-252.53* | *-241.65* | *-241.65* | |
| $r_{max/(W-a)}$=0.35; number of input data points=5005 | | | | | | | | | | |
| $R^2$ | *0.9719* | *0.983* | *0.9861* | *0.9886* | *0.9897* | *0.9901* | *0.9908* | *0.9909* | *0.9909* | |
| $\Delta K$ [MPa×m$^{0.5}$] | *25.04* | *27.74* | *28.38* | *26.86* | *26.13* | *25.55* | *23.97* | *23.74* | *23.94* | *22.22* |
| $\Delta\sigma_0$ [MPa] | *0.00* | *29.52* | *18.28* | *-25.45* | *-51.63* | *-79.70* | *-167.54* | *-183.19* | *-166.40* | |
| $r_{max/(W-a)}$=0.95; number of input data points=35093 | | | | | | | | | | |
| $R^2$ | *0.8083* | *0.862* | *0.9388* | *0.9529* | *0.9766* | *0.9837* | *0.989* | *0.9902* | *0.9905* | |
| $\Delta K$ [MPa×m$^{0.5}$] | *20.07* | *25.91* | *28.19* | *31.67* | *28.45* | *30.64* | *28.72* | *27.22* | *26.28* | *22.22* |
| $\Delta\sigma_0$ [MPa] | *0.00* | *40.71* | *-0.06* | *66.20* | *-10.37* | *57.88* | *-4.51* | *-73.59* | *-127.43* | |

Table 5. Values of SIF and T-Stress for R=-1 from the LSF method ($r_{min}$=5 px; $r_{max}$=18, 24, 43, 116 px).

| Number of Williams' terms | 1 | 2 | 3 | 4 | 5 | 6 | 8 | 10 | 12 | FEM |
|---|---|---|---|---|---|---|---|---|---|---|
| $r_{max/(W-a)}$=0.15; number of input data points=804 | | | | | | | | | | |
| $R^2$ | *-3.3424* | *0.3961* | *0.7913* | *0.9449* | *0.9449* | *0.9459* | *0.9464* | *0.9479* | *0.9479* | |
| $\Delta K$ [MPa×m$^{0.5}$] | *19.31* | *5.00* | *8.74* | *4.95* | *4.95* | *5.28* | *5.62* | *7.59* | *7.59* | *21.78* |
| $\Delta\sigma_0$ [MPa] | *0.00* | *-223.20* | *-259.82* | *-410.38* | *-410.73* | *-388.71* | *-364.06* | *-172.11* | *-172.11* | |
| $r_{max/(W-a)}$=0.20; number of input data points=1508 | | | | | | | | | | |
| $R^2$ | *-1.5263* | *0.4641* | *0.8025* | *0.9581* | *0.9599* | *0.9606* | *0.9608* | *0.9618* | *0.9618* | |
| $\Delta K$ [MPa×m$^{0.5}$] | *19.60* | *6.72* | *10.09* | *5.61* | *5.23* | *5.52* | *5.48* | *7.04* | *7.04* | *21.78* |
| $\Delta\sigma_0$ [MPa] | *0.00* | *-179.88* | *-223.27* | *-383.66* | *-400.90* | *-383.64* | *-388.59* | *-249.31* | *-249.31* | |
| $r_{max/(W-a)}$=0.35; number of input data points=5005 | | | | | | | | | | |
| $R^2$ | *0.1287* | *0.6116* | *0.8268* | *0.9462* | *0.9707* | *0.9712* | *0.9717* | *0.9719* | *0.9721* | |
| $\Delta K$ [MPa×m$^{0.5}$] | *19.63* | *10.82* | *13.46* | *8.22* | *6.48* | *6.18* | *5.54* | *6.22* | *6.81* | *21.78* |
| $\Delta\sigma_0$ [MPa] | *0.00* | *-96.30* | *-142.12* | *-292.28* | *-355.26* | *-369.50* | *-405.67* | *-355.63* | *-307.70* | |
| $r_{max/(W-a)}$=0.95; number of input data points=35093 | | | | | | | | | | |
| $R^2$ | *0.677* | *0.6814* | *0.8419* | *0.8528* | *0.9612* | *0.9615* | *0.9802* | *0.9819* | *0.982* | |
| $\Delta K$ [MPa×m$^{0.5}$] | *17.21* | *16.05* | *18.34* | *16.21* | *11.41* | *11.07* | *7.23* | *5.95* | *5.99* | *21.78* |
| $\Delta\sigma_0$ [MPa] | *0.00* | *-8.09* | *-49.14* | *-89.70* | *-203.65* | *-214.02* | *-347.86* | *-406.91* | *-403.32* | |

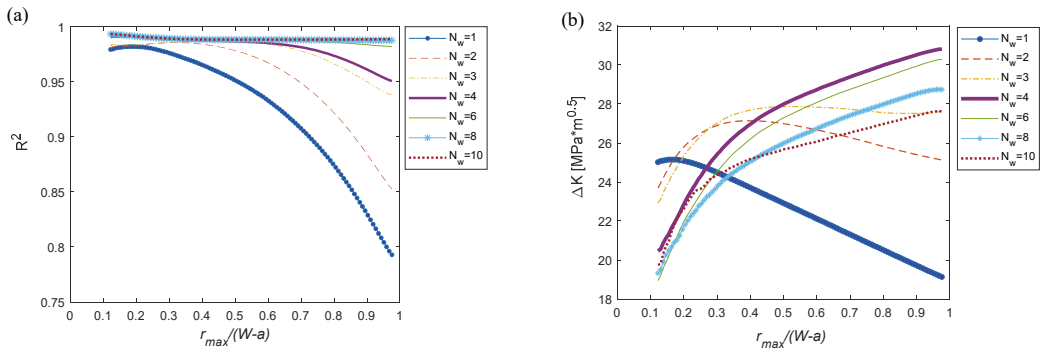


Fig. 7. (a) Evolution of $R^2$ with $r_{max}$ and $N_w$; (b) variation of $\Delta K$ with $r_{max}$ and $N_w$. Both plots are obtained for the case of R=0.1. The data input area has a constant $r_{min}/(w\text{-}a)$=0.04.

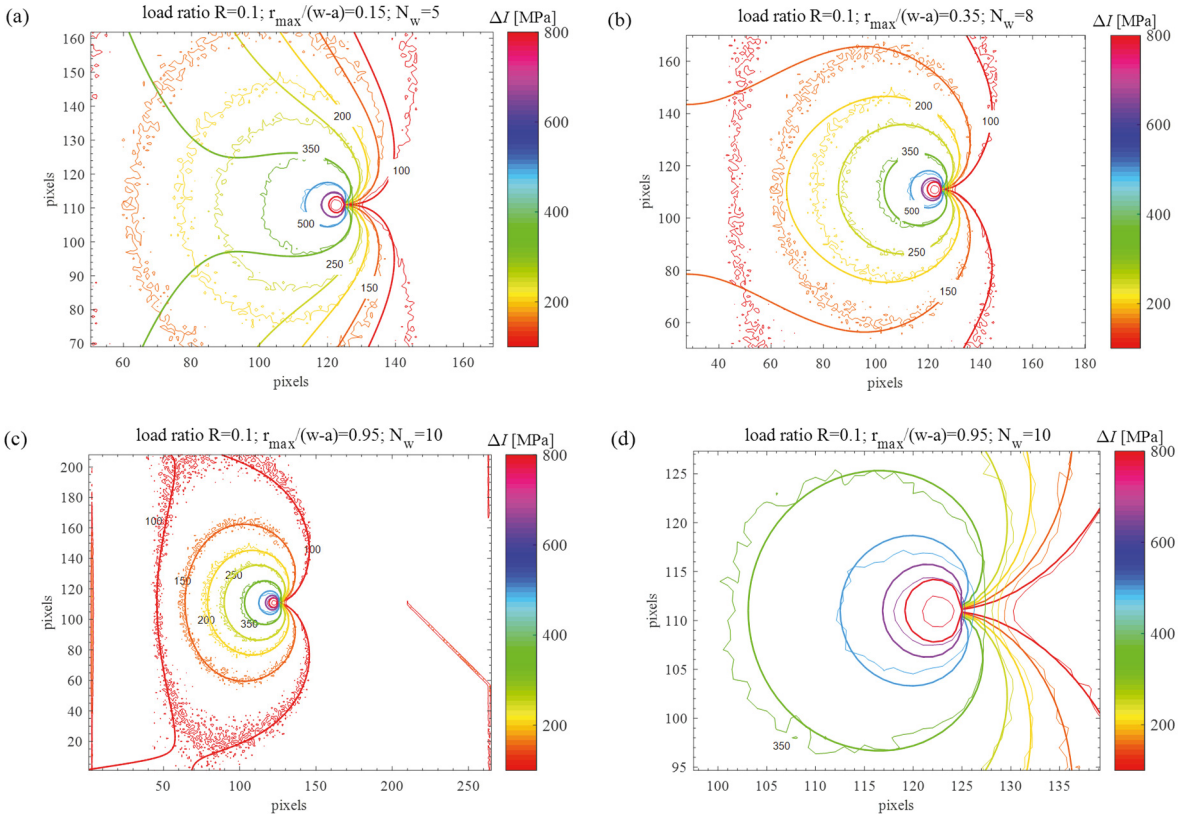


Fig. 8. Contour plot comparison between experimental and least-square fit isopachics for load ratio R=0.1 and various $r_{max}$ and $N_w$.

Comparing the values of $\Delta K$ from R=0.1 and R=0 at equal $r_{max}$ and $N_w$, there seems to be not a significant difference, confirming what already observed with the Stanley-Chan evaluation (section 4.2). A rather relevant difference is instead observed with the case of R=-1. In this case small values of $r_{max}$ yield very low values of $\Delta K$, and in general, there is a much higher variation, ranging between 4 and 20 MPa×m$^{0.5}$. The influence of the half cycle in compression on the isopachic contours, in particular the crack-closure on the wake of the crack, is evident already in Fig. 3c, and has a paramount influence on the least square fitting (see also Fig. 9). It is evident here that the case of fully reversed loading (and R<0 in general) needs further work regarding the possibility to correlate the isopachic data with the stress field and fracture parameters.

Another noteworthy output of the LSF is the evaluation of the T-stress. From the results of Tables 3,4,5 it is seen that this parameter has a very wide range of variation with changing $r_{max}$ and $Nw$. There are very few works in the literature which have reported the value of the T-Stress measured from the thermoelastic signal. In Pukas (1987) a theoretical value of $\sigma_{xo}$=-0.42$\sigma$, with $\sigma$ the remote nominal tension, is indicated for the SENT specimen having $H$=$W$ (with $H$ distance between the grips) and with a relative crack length $a/W$=0.5. This is a similar case to the present one (see Fig. 1), and then it should indicate an expected $\Delta\sigma_{xo}$ of about -26 MPa for R>0. But such value is seldom matched in Tables 3, 4. In the work of Zanganeh et al. (2008) it is shown that the $\Delta\sigma_{xo}$ changes drastically when using 2 or 3 terms in the Williams' series. The same authors pointed out a strong influence of the crack tip location in the evaluation of $\Delta\sigma_{xo}$. Although these authors did not explore higher number of Williams' terms, and did not make an evaluation of the impact of the data input region, their results indicate that the T-stress is indeed very sensitive to the least-square fitting chosen parameters.

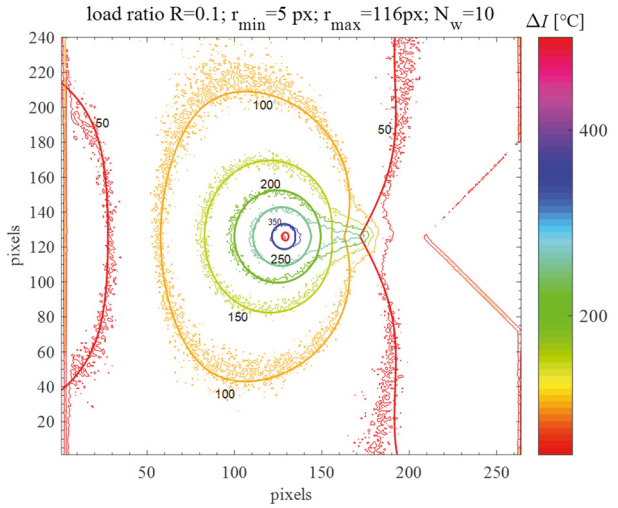


Fig. 9. Contour plot comparison between experimental and least-square fit isopachics for load ratio R=-1.

### *4.4. Interpretation of the Second Harmonic maps*

Second harmonic is the denomination typically found in the literature for the harmonic temperature at twice the loading frequency. This can be easily obtained in terms of range and phase with the same signal processing approaches used for the first harmonic in TSA. A number of different explanations have been proposed to explain the rise of such second harmonic in some circumstances (Jones and Pitt (2006)). Three are in particular the most accredited,

- The strong dependence of the material elastic and physical properties with temperature, which enables the so-called Second Order theory of the Thermoelastic Effect. According to this more accurate formulation, a second harmonic modulation arises, still due to the material elastic volume change;
- Intrinsic material dissipation. This is in particular encountered at incipient plasticity, or other forms of incipient damage. In this case the second harmonic originates by the irreversible heating that is generated twice per load cycle;
- Friction effects between rubbing crack or delamination faces, generating an irreversible heating at each loading/unloading iteration.

In the case of a crack subject to Mode I cyclic loading, a high second harmonic signal has been typically detected in front of the crack tip and in some circumstances along the crack flanks. Jones and Pitt (2006) in particular coupled the second order thermoelastic theory with the crack tip stress field equations and observed that the second harmonic response, as induced by elastic straining, is proportional to 1/r and not $1/\sqrt{r}$, and therefore it is expected to generate a significant signal where the stress gradient is higher. This is possibly added to a plasticity-induced second harmonic.

Regarding the second harmonic signal on the crack flanks, this typically occurs when the load ratio R is negative or near zero. Jones and Pitt (2006) have associated this to rubbing effects, while Bar and Seifert (2014) and Urbanek and Bär (2017) suggest also a correlation with material plasticization. In Ancona et al. (2016) it is also pointed out that the phase map of the second harmonic undergoes a 180° shift between the zones ahead and behind the crack.

The second harmonic maps acquired in this work are reported in Fig. 10-11. At R=0.1 the range $\Delta T$ is surprisingly small and closely localized at the crack tip, while is practically null elsewhere. At R=0 the signal is already more marked, prevalently right behind the crack tip (see also Fig. 11a). At R=-1 the signal is instead well pronounced and characterized by two peak zones, one ahead of the crack and one on the crack flanks. The two zones are also separated by a narrow area of null signal, and each of them is opposite in phase to the other. All such features then confirm previous observations reported in the literature.

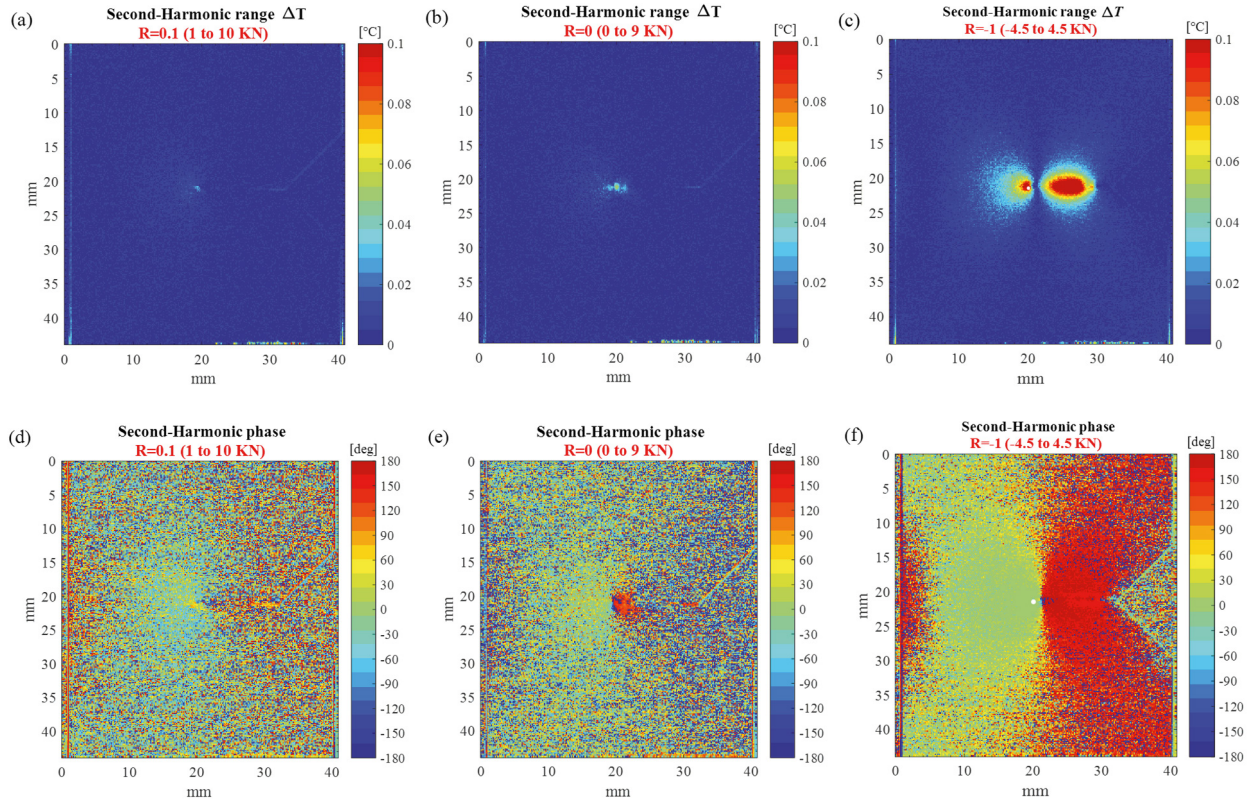


Fig. 10. Second-Harmonic range DT (a,b,c) and phase (d,e,f) maps acquired with load ratios R of 0.1 (a,d), 0 (b,e) and -1 (c,f). The white dot in maps (c,f) indicates the crack-tip location measured by optical camera. The data reported are obtained from tests with load frequency 15 H.

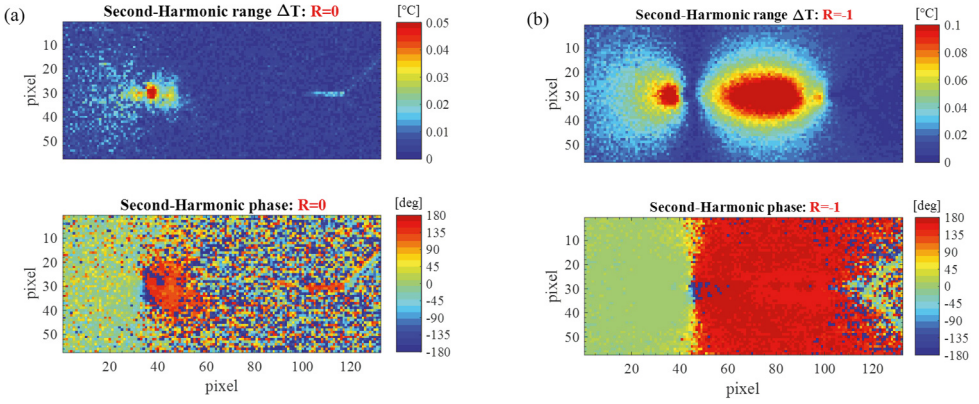


Fig. 11. Close-up of Second-Harmonic response for R=0 and R=-1.

In this work a new explanation is given to reveal the nature of the Second Harmonic signal on the crack flanks.

Lets assume that the force acting on the crack flanks corresponds to the half-cycle in compression of the sinusoidal load. Figure (12) shows a scheme with the two varying signals, the fully reversed sinusoidal signal (blue curve) represents the load acting on the ligament in front of the crack; the half cycled signal (curve in red) is a simplified representation of the load experienced by points near the crack flanks.

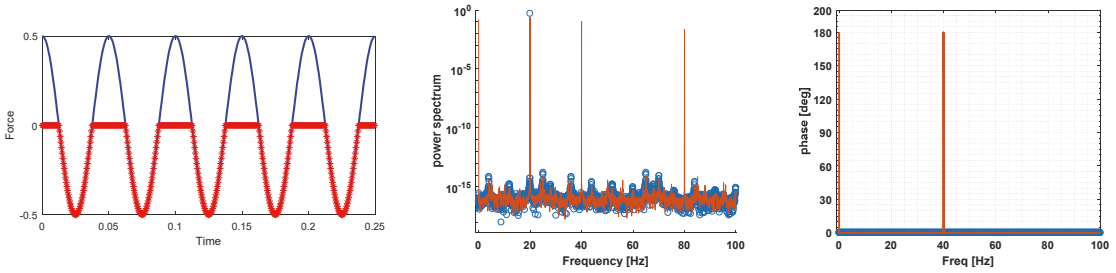


Fig. 12. (a) Schematic representation of the loads acting on internal points (curve in blue) and points lying on the crack flanks (curve in red); (b) Power spectrum and (c) phase spectrum from the DFT of the blue and red loading curves.

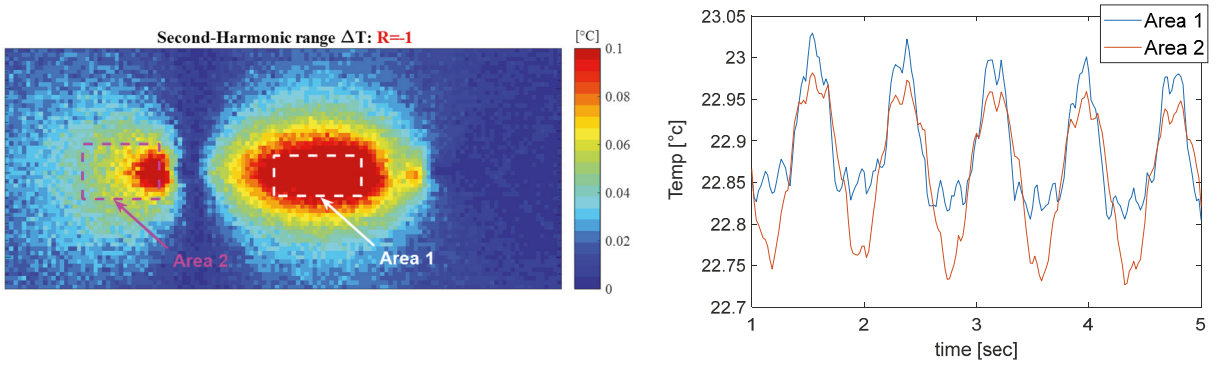


Fig. 13. (a) Areas selected for the plot (b) of average temperature versus time.

By performing the Discrete Fourier Transform on the blue and red curves of Figure 12a, one obtains the power spectrum and phase spectrum shown in Figure 12b,c. It is in particular found that the red curve has three main harmonics at ω=20, 2ω=40 and 4ω=80 Hz, while the blue curve has only one harmonic at ω=20 Hz (the time scale is here assumed to be [sec]). Furthermore, the harmonic of the red curve at 20 Hz is in phase with the external load (blue dots in Fig. 12a), while the harmonic of the red curve at 40 Hz is shifted by 180 °. These harmonics at ω and 2ω act as two different external cyclic loads, applied simultaneously. For simplicity, from now on, the external load related to the blue curve is indicated as L, and the two loading components related to the red curve are indicated as $L_1$ and $L_2$.

By transferring the above scheme into the case of Figure 10c,f and 11, it emerges that the first harmonic signal on the crack flanks is a thermoelastic signal induced by the $L_1$ loading component, and the second harmonic signal on the crack flanks is still a thermoelastic signal but this time associated to the $L_2$ loading component. The loading scheme of Fig. 12a explains also why the first harmonic signal is in phase with the signal ahead of the crack-tip (see Fig. 3f), while the second harmonic is opposite in phase.

It is observed that the above behaviour is determined every time the crack flanks come into contact and press against each other, therefore the same features of the second harmonic can be associated also to the presence of crack-closure, other than negative load ratios R. Indeed, in the case of R=0 in Fig. 11a, the presence of a significant second harmonic right behind the crack is most likely attributable to a localised crack-closure.

The narrow band of null signal in the second harmonic map, separating the crack flanks from the ligament, has been interpreted by some authors as a zone with a lack of contact between the crack flanks (see e.g. Jones and Pitt (2006)). In this work instead, this null band is explained as the consequence of a gradual change in the phase shift from 180° to 0° (or vice versa, according the reference chosen for 0° phase), requiring the amplitude to pass from zero.

A final proof that can further validate the above explanation is provided in Fig. 13. Here a rectangular area is taken across the crack flanks, in the second harmonic map. The average temperature from this area is then plotted versus

time in fig. 13b. The plot shows clearly how the temperature follows a similar modulation as the one given to the red load curve in Fig. 12a. The temperature also lies on the positive semi-plane, and is opposite in sign with the generating compression load.

## 5. Conclusions

In this work a Thermoelastic Stress Analysis setup has been implemented to evaluate the *Thermoelastic* and *Second Harmonic* signals from a *Single Edge Notched Tension* sample made of stainless steel AISI 304L, subject to fatigue cyclic loading with load ratios $R$=-1, 0, 0.1.

The maps of the thermoelastic signal have been analyzed to evaluate the Stress Intensity Factor (SIF) and T-Stress. The Stanley-Chan linear fitting procedure has provided values of SIF higher than the FEM prediction for $R$-ratios of 0 and 0.1. It is observed that considering the influence of a negative T-Stress, neglected in the Stanley-Chan interpolation, would yield smaller values of SIF. Results from the Stanley-Chan evaluation also showed a tendency of the SIF to diminish with decreasing load ratio $R$, which could be ascribed to the influence of crack closure and the onset of a reduced effective SIF.

The least-square fitting based on the Williams' stress function has indicated that there is a convergence of results for a number of terms higher than ten. A coefficient of determination $R^2$ has been used to evaluate the quality of fitting. Using such parameter and iterating the least square fitting has allowed to select an optimized position of the crack tip on the thermoelastic maps, which agreed well with the evaluation made by accurate optical measures. Regarding the SIF and T-Stress results, these have been found to be significantly influenced by the extension and position of the area used as input data, and by the number of terms considered in the series function. It is observed in general that extending the data input area has an overall effect of improving the fitting, but the local fitting in the zones with steepest gradients near the crack tip is worsened. On the contrary, smaller data input areas, closer to the crack tip, improve the fitting near the crack tip but are not able to satisfactory model the isopachics further out. More work is needed to establish a criterion able to identify the optimal data input area extension and position in order to have the most reliable evaluation of the SIF and T-Stress.

This study has also investigated the features of the Second Harmonic signal in terms of both amplitude and phase. In particular, a peculiar shape of the Second Harmonic amplitude has been identified with load ratios of $R$=-1 and 0, which has been correlated with the presence of crack closure. In particular, the high Second Harmonic signal on the wake of the crack has been explained as a thermoelastic signal component that happens to be modulated at twice the loading frequency. This occurs due to the peculiar wave shape of the compression load acting on the crack flanks. The arising compression load generates a local thermoelastic signal which is compatible with the amplitude and phase features shown by the Second Harmonic signal. This interpretation somewhat revises other explanations found in the literature, which associate the Second Harmonic signal to dissipation and frictional effects. Moreover, the given interpretation allows to propose the Second Harmonic as an effective parameter to reveal the presence and the extent of crack-closure.

## Acknowledgements

The IR thermal camera FLIR X6540sc used in this work has been purchased using funds from the project INTEP – PO FESR 2007/2013 – 4.1.2.A.

## References

Alshaya, A. and Rowlands, R., 2017. Experimental Stress Analysis of a Notched Finite Composite Tensile Plate. Composites Science and Technology 144, 89–99.

Ancona, F., De Finis, R., Demelio, G.P., Galietti, U., Palumbo, D., 2016. Study of the Plastic Behavior around the Crack Tip by Means of Thermal Methods. Procedia Structural Integrity 2, 2113–22.

Ancona, F., Palumbo, D., De Finis, R., Demelio, G.P., Galietti, U., 2016. Automatic Procedure for Evaluating the Paris Law of Martensitic and Austenitic Stainless Steels by Means of Thermal Methods. Engineering Fracture Mechanics 163, 206–19.

Bar, J, and Seifert, S., 2014. Thermographic Investigation of Fatigue Crack Propagation in a High-Alloyed Steel. Advanced Materials Research 892, 936–41.

Díaz, F.A., Yates, J.R., Patterson, E.A., 2004a. Some Improvements in the Analysis of Fatigue Cracks Using Thermoelasticity. International Journal of Fatigue 26 (4), 365–76.

Diaz, F.A., Patterson, E.A., Tomlinson, R.A., Yates, J.R., 2004b. Measuring Stress Intensity Factors during Fatigue Crack Growth Using Thermoelasticity. Fatigue & Fracture of Engineering Materials & Structures 27 (7), 571–83.

Dulieu-Barton, J. M., Fulton, M.C., Stanley, P., 2000. Analysis of Thermoelastic Isopachic Data from Crack Tip Stress Fields. Fatigue and Fracture of Engineering Materials and Structures 23 (4), 301–13.

Fett, T., 1998. A Compendium of T-Stress Solutions. Forschungszentrum Karlsruhe, Wissenschaftliche Berichte. FZKA.

Haj-Ali, R., Wei, B.S., Johnson, S., El-Hajjar, R., 2008. Thermoelastic and Infrared-Thermography Methods for Surface Strains in Cracked Orthotropic Composite Materials. Engineering Fracture Mechanics 75 (1), 58–75.

He, K.Y. and Rowlands, R.E., 2004. Determining Stress Intensity Factors in Orthotropic Composites from Far-Field Measured Temperatures. Experimental Mechanics 44 (6), 555–61.

Jones, R., Krishnapillai, M., Cairns, K., Matthews, N., 2010. Application of Infrared Thermography to Study Crack Growth and Fatigue Life Extension Procedures. Fatigue and Fracture of Engineering Materials and Structures 33 (12), 871–84.

Jones, R., and Pitt, S., 2006. An Experimental Evaluation of Crack Face Energy Dissipation. International Journal of Fatigue 28 (12), 1716–24.

Ju, S.H., Chiu, C.Y., Jhao, B.J., 2010. Determination of SIFs, Crack-Tip Coordinates and Crack Angle of Anisotropic Materials. Fatigue and Fracture of Engineering Materials and Structures 33 (1), 43–53.

Ju, S.H., Lesniak, J.R., Sandor, B.I., 1997. Numerical Simulation of Stress Intensity Factors via the Thermoelastic Technique. Experimental Mechanics 37 (3), 278–84.

Lesniak, J.R. and Boyce, B.R., 1995. Differential Thermography Applied to Structural Integrity Assessment. In SPIE 2473, Thermosense XVII, An International Conference on Thermal Sensing and Imaging Diagnostic Applications, 2473, 2411–73.

Lin, S.J., Samad, W.A., Khaja, A.A., Rowlands, R.E., 2015. Hybrid Thermoelastic Stress Analysis. Experimental Mechanics 55 (4), 653–65.

Lin, S.T., Feng, Z., Rowlands, R.E., 1997. Thermoelastic Determination of Stress Intensity Factors in Orthotropic Composites Using the J-Integral. Engineering Fracture Mechanics 56 (4), 579–92.

Meneghetti, G., Ricotta, M., Atzori, B., 2016. A Two-Parameter, Heat Energy-Based Approach to Analyse the Mean Stress Influence on Axial Fatigue Behaviour of Plain Steel Specimens. International Journal of Fatigue 82, 60–70.

Meneghetti, G., Ricotta, M., Pitarresi, G., 2019. Infrared Thermography-Based Evaluation of the Elastic-Plastic j-Integral to Correlate Fatigue Crack Growth Data of a Stainless Steel. International Journal of Fatigue, 125, 149-160.

Meneghetti, G. and Lazzarin, P., 2007. Significance of the Elastic Peak Stress Evaluated by FE Analyses at the Point of Singularity of Sharp V-Notched Components. Fatigue & Fracture of Engineering Materials & Structures 30 (2), 95–106.

Palumbo, D., De Finis, R., Ancona, F., Galietti, U., 2017. Damage Monitoring in Fracture Mechanics by Evaluation of the Heat Dissipated in the Cyclic Plastic Zone Ahead of the Crack Tip with Thermal Measurements. Engineering Fracture Mechanics 181, 65–76.

Pitarresi, G., 2015. Lock-In Signal Post-Processing Techniques in Infra-Red Thermography for Materials Structural Evaluation. Experimental Mechanics 55 (4), 667–80.

Pitarresi, G. and Patterson, E.A., 2003. A Review of the General Theory of Thermoelastic Stress Analysis. The Journal of Strain Analysis for Engineering Design 38 (5), 405–17.

Pukas, S.R., 1987. Theoretical Considerations For Determining Stress Intensity Factors Via Thermoelastic Stress Analysis. In Proc. SPIE 0731, Stress Analysis by Thermoelastic Techniques, 0731, 88–101.

Ramesh, K., Gupta, S., Kelkar, A.A., 2002. Evaluation of Stress Field Parameters in Fracture Mechanics by Photoelasticity—Revisited. Engineering Fracture Mechanics 56 (1), 25–45.

Stanley, P. and Dulieu-Smith, J.M., 1996. The Determination of Crack-Tip Parameters from Thermoelastic Data. Experimental Techniques 20 (2), 21–23.

Stanley, P, and Chan, W.K., 1986. The Determination of Stress Intensity Factors and Crack-Tip Velocities from Thermoelastic Infra-Red Emissions. In Proceedings International Conference on Fatigue of Engineering Materials and Structures (I.Mech.E.), Sheffield, UK, 105–14.

Tomlinson, R.A. Olden, E.J., 1999. Thermoelasticity for the Analysis of Crack Tip Stress Fields - a Review. Strain 35 (2), 49–55.

Tomlinson, R.A., Nurse, A.D., Patterson, E.A., 1997a. Mixed Mode Cracks From Thermoelastic Data. Fatigue & Fracture of Engineering Materials & Structures 20 (2), 217–26.

Tomlinson, R.A., Nurse, A.D., Patterson, E.A., 1997b. On determining stress intensity factors for mixed mode cracks from thermoelastic data. Fatigue & Fracture of Engineering Materials & Structures 20 (2), 217–26.

Urbanek, R. and Bär, J., 2017. Influence of Motion Compensation on Lock-In Thermographic Investigations of Fatigue Crack Propagation. Engineering Fracture Mechanics 183, 13–25.

Vieira, R.B., Gonzáles, G.L.G., Freire, J.F.L., 2018. Thermography Applied to the Study of Fatigue Crack Propagation in Polycarbonate. Experimental Mechanics 58 (2), 269–82.

Zanganeh, M., Tomlinson, R.A., Yates, J.R., 2008. T-Stress Determination Using Thermoelastic Stress Analysis. Journal of Strain Analysis for Engineering Design 43 (6), 529–37.